Mechanics of Materials 196 (2024) 105079

Contents lists available at ScienceDirect

Mechanics of Materials

journal homepage: www.elsevier.com/locate/mechmat

Research paper

# A mechanistic interpretation of Nelson curves for PVP failures under high temperature hydrogen attack

Dong Han [a], Yanfei Gao [a,*], Phillip E. Loya [b], Michael Swindeman [c], Jorge Penso [d], Zhili Feng [e,**]

[a] Department of Materials Science and Engineering, University of Tennessee, Knoxville, TN, 37996, USA
[b] Stress Engineering Services Inc, Houston, TX, 77041, USA
[c] Stress Engineering Services Inc, Mason, OH, 45050, USA
[d] Shell Global Solution (US) Inc, TX, 77082, USA
[e] Materials Science and Technology Division, Oak Ridge National Laboratory, Oak Ridge, TN, 37831, USA

ARTICLE INFO

Handling Editor: Prof. G Subhash

*Keywords:*
Nelson curves
High temperature hydrogen attack (HTHA)
Microstructure-informed and micromechanics-based model
Intergranular fracture

ABSTRACT

As an empirically established design criterion, Nelson curves that relate the service temperature and the allowable hydrogen partial pressure have been developed and utilized for more than sixty years in pressure vessels and piping (PVP) safety design. Despite a relatively clear thermodynamic understanding of the high-temperature-hydrogen-attack (HTHA) problem, the detailed fracture process on the microstructural length scales, however, remains elusive, and a quantitative assessment of the PVP lifetime under HTHA from the available creep fracture dataset is still not possible. This work develops a microstructure-informed and micromechanics-based model by incorporating a synergy between hydrogen transport and intergranular-cavity-based fracture process. Based on the available creep lifetime data of C-0.5Mo steels, we are able to calibrate material constitutive parameters, and then conduct nonlinear finite element simulations that reveal a real-time stress-induced hydrogen diffusional transport along grain boundaries, coupled with a microstructure-explicit failure process, from which Nelson curves can be computed. Such failure analyses allow us to delineate two distinct regimes on the Nelson curves, i.e., dislocation-creep-controlled or grain boundary diffusion-assisted cavity growth. More importantly, we found that a small change of the pipe thickness and applied stresses can significantly shift these lifetime curves. However, these two parameters are usually not provided in Nelson curves, thus limiting their usage in material selection and safety design. This discrepancy can clearly be mitigated by extensive parametric studies from our micromechanical modeling/simulation framework.

## 1. Introduction

High temperature hydrogen attack (HTHA), bringing the permanent/irreversible deterioration of mechanical properties of petroleum refinery and petrochemical plant equipment fabricated mostly by carbon and low alloy steels, has always been of the major concern to the pressure vessels and piping (PVP) community (American Petroleum Institute, 2016; Nelson and Beachem, 1977). As a very complicated mechanical-physical-chemical process, HTHA entails absorption of hydrogen from the surface of steels, diffusion of hydrogen atoms along grain boundaries, formation of methane resulting from chemical reaction between hydrogen and carbon (interstitial ones or from carbides in the microstructure) and growth of cavities driven by applied stresses and internal pressure due to the accumulation of the methane gas (Bharadwaj, 2015). The growth of cavities can be promoted by local creep processes, i.e., diffusion of atoms along grain boundaries and dislocation creep in the adjacent grains. And fissures typically form and grow upon the growth and coalescence of cavities and finally results in a macroscopic intergranular fracture (Parthasarathy, 1985; Shewmon, 1987a).

In early attempts, by collecting data from reported HTHA failures, HTHA-damaged but non-failed components and several cases of satisfactory operation of HTHA on different steels, a set of curves, known as "Nelson curves", are developed to assess the susceptibility to HTHA and establish the safe operating limits for carbon and low-alloy steels in high temperature and high-pressure hydrogen (American Petroleum Institute, 2016; Nelson and Beachem, 1977). The American Petroleum

* Corresponding author.
** Corresponding author.
*E-mail addresses:* ygao7@utk.edu (Y. Gao), fengz@ornl.gov (Z. Feng).

https://doi.org/10.1016/j.mechmat.2024.105079
Received 13 November 2023; Received in revised form 13 May 2024; Accepted 21 June 2024
Available online 24 June 2024
0167-6636/© 2024 Elsevier Ltd. All rights are reserved, including those for text and data mining, AI training, and similar technologies.

Institute (API) maintains and offers updated Nelson curves through Recommended Practice (RP) 941 (American Petroleum Institute, 2016), which serve as an authoritative guide for safe material choice to avoid the occurrence of HTHA. As a representative example, Nelson curves of C-0.5Mo steel are given in Fig. 1(a). Based on hydrogen partial pressure, material compositions and temperature, operational conditions can be divided into non-damaged and damaged regimes with certain lifetimes labeled on these Nelson curves. Experimental data have been collected that clearly show the bottom left regime being the safe operating conditions. Although this approach has found some successes in safety design due to its simplicity, the usage of Nelson curves is only restricted to a small number of commonly used steels. On the other hand, a more complete creep lifetime database exists, such as those provided by National Institute of Materials Research (NIMS), Japan (National Institute of Materials Research (NIMS) and Japan, 2003). A question that naturally arises is whether we can predict such Nelson curves from the extensive creep experiments and the studies of hydrogen thermodynamics/kinetics.

Aiming to turn empirical Nelson curves to mechanistic ones, we start from the Sherby-Dorn equation (Nieh et al., 1997) for creep fracture lifetime, given by

$$t_r = Ap^{-n} \exp(Q/RT), \tag{1}$$

where $t_r$ represents the time to a particular damage state, such as incubation, cracking or failure, $A$ is a material constant depending on the properties of steels, $p$ is the applied stress, and $Q$ is the activation energy reflecting the dominant deformation mechanism (e.g., dislocation creep or grain boundary diffusion). Rearranging Eq. (1) to a logarithmic form gives

$$\ln t_r = -n \ln p + \frac{Q}{RT} + \ln A, \tag{2}$$

$$\ln p = \frac{Q}{nRT} + \frac{\ln A - \ln t_r}{n}. \tag{3}$$

Now replot Nelson curves in Fig. 1(a) with respect to the hydrogen partial pressure and the reciprocal of temperature as shown in Fig. 1(b). If we blindly take $p$ as the hydrogen partial pressure, we should see linear or piece-wise linear curves with the slopes being $Q/nR$. These converted Nelson curves do not show such geometric features, and even an intentional curve fitting will give a $Q$ value that is one order of magnitude smaller than the creep measurements. In contrast, the creep fracture dataset will clearly demonstrate two straight lines, one being controlled by grain boundary diffusion at high temperature and low stress, and the other by dislocation creep at intermediate temperature and high stress. The slopes can be used to obtain the activation energies.

The failure of the Sherby-Dorn equation in Fig. 1(b) suggests that the first step in understanding Nelson curves lies with the thermodynamics and kinetics of hydrogen, including hydrogen adsorption on the PVP inner diameter (ID), hydrogen transport into the bulk through grain boundaries, and then reaction and formation into methane. These thermodynamic and kinetic processes are fairly understood as will be summarized in Section 2, which will convert the hydrogen partial pressure into a total pressure (consisting of hydrogen and methane) that plays the same role of the applied stress. As will be demonstrated later, there still exist considerable discrepancies between the converted Nelson curves using the total pressure and the creep fracture dataset. The missing link clearly lies on the actual microstructure-based failure processes.

Important earlier investigations into HTHA failure processes can be grouped into cavity nucleation and growth models (Vitovec, 1984; Sundararajan and Shewmon, 1981). Of these two, growth models are more sophisticated and capable of predictions within an order of magnitude in comparison to experiments (Sundararajan and Shewmon, 1981). They consider methane production rate (represented by a function of cavity size/volume) and either unconstrained or constrained cavity growth by creep. For a single cavity contained within a cylindrical or a spherical unit cell, analytical relations have been attempted for both diffusive and creep-constrained cavity growth modes. For example, Shih and Johnson (1982) applied a void growth model that involved methane reaction kinetics to calculate the Nelson curve for plain carbon steel. Methane pressure was considered the driving force for void growth, which was considered to be dominated by grain-boundary diffusion at the early stage and later by creep. Noting that methane fugacity in bubbles is significantly higher than methane pressure, Odette and Vagarali (1982) presented an "equation-of-state" for a better assessment of methane pressure (in carbon steel), which is necessary for a successful modeling. Later, the synergy between creep deformation due to external stress and grain boundary cavitation due to methane bubble growth was numerically investigated by Shewmon (1987b). Based on Odette-Vagarali model (Odette and Vagarali, 1982) for methane pressure calculation, Van der Burg, Van der Giessen and colleagues (Van der Burg and Van der Giessen, 1997; Van der Burg et al., 1998; Van der Burg and Van der Giessen, 1996; D Van der Burg et al., 1996) calculated HTHA damage and the remaining life of the component in HTHA-susceptible service by adding model for the growth and coalescence of grain-boundary cavities under macro-scale stress. The model was used for the calculation of the Nelson curves. Schlögl and Van der Geissen (Schlögl and Van der Giessen, 2002) used finite element method (FEM) to present a more general numerical microstructure model which is based on a variational approach that coupled two processes, namely carbon diffusion in ferrite and the chemical reaction between hydrogen and carbon to form methane. Dadfarnia et al. (2019) also presented "a simple (one-dimensional) constraint-based model" by improving the mechanistic models of 1980s. They established Nelson-type curves for the material at different levels of stress; the curves were no longer merely phenomenological (i.e., safe vs. unsafe), but showed time to failure. Using a damage mechanics approach, Chavoshi et al. (2020)

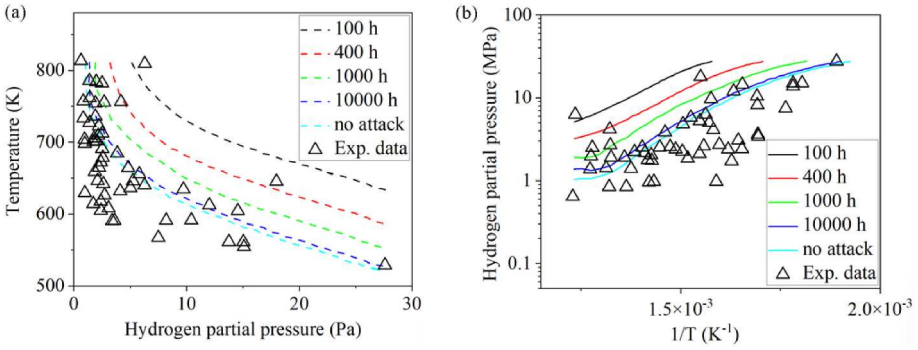


**Fig. 1.** (a) Nelson curves and experimental data for pressure vessels and piping (PVP) of C-0.5Mo ferritic steel (American Petroleum Institute, 2016; Nelson and Beachem, 1977). (b) Replotted Nelson curves with respect to the hydrogen partial pressure and the reciprocal of temperature.

presented a continuum damage mechanics model that combined creep and HTHA damage to evaluate a C-0.5Mo steel after 80,000 h at 350–500 °C and under a hydrogen pressure of 4 MPa. They used hydrogen fugacity and a coupling between Fick's diffusion law and a multi-axial creep ductility model, whereas the ratio of certain strain measure to this ductility defines the damage parameter.

Among the above literature works, finite element simulations are mostly compared to fracture morphology (e.g. (Chavoshi et al., 2020)), and analytical models of single cavities focus on carbon/hydrogen diffusion and growth rate (e.g. (Schlögl and Van der Giessen, 2002)). While the latter has been compared to Nelson curves with some successes, these models essentially do not have a hydrogen gradient over a length scale larger than the grain size. Important features such as the applied load (and its distribution) and the PVP wall thickness are not considered in these literature studies. All these limitations prevent us from predicting Nelson curves from available information, including microstructure, loading conditions, creep dataset, and hydrogen thermodynamics and kinetics with the known material composition.

The objective of this study is to establish a mechanistic explanation of the Nelson curves with the focus on the discrepancies between such an empirical model and the available creep data. The main hypothesis is that combining the well-established thermodynamic model for hydrogen reaction/transport with the creep lifetime data will not be able to quantitatively explain Nelson curves. Instead, with a micromechanical constitutive framework that can be implemented in a nonlinear finite element method (FEM), we can simulate the critical roles played by microstructural information, which eventually identifies the gaps to the prediction of Nelson curves. In Section 2, the thermodynamic and kinetic processes governing the reaction and transport of hydrogen will be reviewed. Section 3 discusses a smear-out model that links the responses of individual cavities to the grain boundary fracture. Both diffusive and creep-constrained cavity growth models will be incorporated in the FEM model that explicitly captures the failure processes on the microstructural length scale, as explained in Section 4. Calibrated from NIMS creep strain-rate and lifetime data (National Institute of Materials Research (NIMS) and Japan, 2003), our microstructure-explicit failure model can predict Nelson curves under arbitrary geometric and loading conditions. Subsequently, the gradients in hydrogen concentration and load distributions are systematically studied, and our nonlinear FEM simulations reveal the drastic shift of these Nelson curves with the change of applied stress and PVP thickness. Implications of these findings will be discussed with respect to the uniqueness of Nelson curves and their predictive capabilities in Section 5. The concluding remarks will be given in Section 6.

## 2. Thermodynamic and kinetic processes

The adsorption, transport, and reaction of hydrogen with many steel alloys have been well understood. Since our objective is on the microstructure-based failure processes, we rather restrict this work to C-0.5Mo steel, which is a ferritic steel commonly used under high temperature conditions. With optimal heat treatment, the combination of solid solution strengthening due to Mo alloying and precipitation strengthening upon tempering results into the needed creep resistance. Discussions in this section primarily follow the Odette-Vagarali model (Odette and Vagarali, 1982).

### 2.1. Hydrogen adsorption

When the PVP inside surface is exposed to a hydrogen-rich environment, hydrogen atoms can be adsorbed onto the steel surface. The thermodynamic equilibrium between hydrogen gas and dissolved atomic hydrogen is expressed by the general form of Sieverts Law (Sieverts, 1935)

$$c_{\mathrm{H}} = S(T) f_{\mathrm{H_2}}^{1/2}, \tag{4}$$

where $c_{\mathrm{H}}$ and $S(T)$ are the equilibrium hydrogen concentration and the equilibrium solubility of hydrogen gas, respectively. Given that the solution is also affected by the hydrostatic pressure in the steels, $S(T)$ can be described as

$$S(T) = S_0 \exp[(-\Delta G - p\overline{V}_{\mathrm{H}})/RT]. \tag{5}$$

Here $S_0$ is the solubility coefficient. $\Delta G$ is the activation energy for solubility. $p$ is the hydrostatic pressure in the steel. And $\overline{V}_{\mathrm{H}}$ is the partial molar volume of hydrogen in iron-based alloys. $f_{H_2}$ is the equilibrium hydrogen fugacity and given as a function of hydrogen partial pressure (Van der Burg and Van der Giessen, 1997),

$$f_{\mathrm{H_2}} = P_{\mathrm{H_2}} \exp[P_{\mathrm{H_2}} \bullet y(T)], \tag{6}$$

$$y(T) = 1.54 \times 10^{-6}\mathrm{Pa}^{-1} \bullet \mathrm{K}/(\mathrm{T} + 459.67\mathrm{K}) + 4.69 \times 10^{-11}\mathrm{Pa}^{-1}. \tag{7}$$

### 2.2. Hydrogen diffusion

After adsorption, hydrogen can penetrate the steel material itself. Hydrogen atoms, being relatively small and light, can diffuse through the metal lattice. The diffusion can occur through different paths: lattice diffusion, grain boundary diffusion and dislocation and defect (such as vacancies and inclusions) diffusion. Numerous studies and models such as Fisher's classical model (Fisher, 1951) and Whipple's analytical model (Whipple, 1954), indicate that the diffusivity of impurities (like hydrogen) along grain boundaries can be several orders of magnitude, e.g., $10^5 \sim 10^8$, higher than the bulk diffusivity. Thus, the diffusion process in non-preferred paths (like bulk or grains) is always neglected in the studies of corrosion assisted fracture.

Therefore, the diffusion equation can be expressed as a one-dimensional form since only diffusion along grain boundary path is considered in our model. Considering that hydrogen diffusion is driven by gradients of concentration and local pressure, the diffusion equation can be written as,

$$\frac{\partial c_{\mathrm{H}}}{\partial t} = D(T)\left(\nabla^2 c_{\mathrm{H}} + \frac{\overline{V}_{\mathrm{H}}}{RT}\nabla c_{\mathrm{H}} \bullet \nabla p + \frac{\overline{V}_{\mathrm{H}} c_{\mathrm{H}}}{RT}\nabla^2 p\right), \tag{8}$$

where $D(T)$ is the diffusion coefficient of hydrogen as a function of the temperature,

$$D(T) = D_0 \exp[-\Delta E/RT]. \tag{9}$$

Here $D_0$ and $\Delta E$ are diffusion coefficient and activation energy for diffusion separately. And the stress gradient will be evaluated through mechanical responses, as will be discussed later.

### 2.3. Reaction with carbides

As the reverse of adsorption, desorption of hydrogen, namely the release of hydrogen atoms or molecules previously adsorbed onto or within the steels or surface, is inclined to happen during the diffusion of hydrogen atoms. This process can be driven by factors like increased temperature or reduced pressure. In the steels, the diffused hydrogen atoms usually recombine to form hydrogen molecules inside voids, cracks, or imperfections on grain boundaries. Therefore, Sieverts Law and Eq. (3) and Eq. (4) can also be applied to desorption of hydrogen. As hydrogen atoms and molecules amass inside or near inside voids, cracks, or imperfections, carbides tend to react with hydrogen to form methane. Due to the large size, it is not feasible for methane to easily diffuse through the steels. It builds up at the above sites, forms bubbles/cavities, and results in the increasingly large internal pressure. Driven by the methane pressure, the growth and coalescence of these bubbles leads to the deterioration and eventually failure.

A typical reaction between hydrogen gas and carbides is

$$M_xC_y + 2yH_2 \rightleftarrows yCH_4 + xM. \tag{10}$$

Based on the definition of the equilibrium constant $K_0$ of a chemical reaction, the fugacity of methane $f^e_{CH_4}$ can be derived from the hydrogen partial pressure $P_{H_2}$ as

$$f^e_{CH_4} \approx K_0 \bullet P^2_{H_2}, \tag{11}$$

where the specific value of $K_0$ depends on the type of carbide. For cementite it is approximately (Odette and Vagarali, 1982)

$$K_0 = 1.6 \times 10^{-6} \exp\left(\frac{113640}{RT}\right) \mathrm{MPa}^{-1}. \tag{12}$$

Similar to Eq. (3), Odette et al. (Odette and Vagarali, 1982) linked the equilibrium methane pressure and the fugacity of methane by an implicit relationship

$$f^e_{CH_4} = P_{CH_4} \exp\left[P_{CH_4} \bullet C(T)\right], \tag{13}$$

here $P_{CH_4}$ is the methane partial pressure. And a simplification for $C(T)$ is

$$\begin{cases} C(T) = 0.005\,\mathrm{MPa}^{-1} \quad \text{for } f^e_{CH_4} < 10^3\,\mathrm{MPa} \\ C(T) = \dfrac{1.1875}{T} + 3.0888 \times 10^{-3}\,\mathrm{MPa}^{-1} \quad \text{for } 10^3\,\mathrm{MPa} < f^e_{CH_4} < 10^4\,\mathrm{MPa} \\ C(T) = \dfrac{2.375}{T} + 1.1776 \times 10^{-3}\,\mathrm{MPa}^{-1} \quad \text{for } f^e_{CH_4} > 10^4\,\mathrm{MPa} \end{cases}, \tag{14}$$

which is used to predict the methane pressure for various temperature-pressure.

## 3. Creep fracture model

High temperature failure has three representative modes: rupture, intergranular creep fracture and transgranular creep fracture, as illustrated on the fracture mechanism map (Gandhi and Ashby, 1979; Zhang et al., 2020). The most common intergranular creep fracture occurs at grain boundaries at elevated temperature and relatively low stress. Driven by stress and strain concentrations, cavities on grain boundaries tend to nucleate and then grow, which is heavily affected by the competition of dislocation creep in the surrounding grains, grain boundary diffusion, and viscous grain boundary sliding. Subsequently, the coalescence of these cavities can finally lead to grain boundary microcracks. In the end, intergranular failure occurs after the linking-up of neighboring microcracks (Argon, 1983; Cocks and Ashby, 1982; Riedel, 2014).

### 3.1. Deformation model

We presume plastic deformation is dominated by dislocation (power-law) creep in grains, and total strain rate includes elastic strain rate and creep rate, which can be individually conveyed by

$$\dot{\varepsilon}^e_{ij} = \frac{1+\nu}{E}\left(\dot{\sigma}_{ij} - \frac{\nu}{1+\nu}\dot{\sigma}_{kk}\delta_{ij}\right), \tag{15}$$

$$\dot{\varepsilon}^p_{ij} = A_{dis}\frac{EbD_l}{k_B T}\left(\frac{\sigma_e}{\sigma_0}\right)^n \frac{3S_{ij}}{2\sigma_e}\overline{M}^I. \tag{16}$$

In the two equations, $\nu$ is Poisson's ratio and $E$ is Young's modulus separately. $\delta_{ij}$ represents the Kronecker delta; $k_B$ is the Boltzmann's constant; $b$ is the Burgers vector; $T$ is the absolute temperature; $\sigma_e$ is the von Mises stress; $n$ is the stress exponent; $\sigma_0$ is the reference stress; $A_{dis}$ is the material constant; $D_l$ is the diffusivity coefficient for the dislocation. And the normalized micromechanical Taylor factor for the $I_{th}$ grain $\overline{M}^I = M^I/\max\left(M^1, M^2, \ldots, M^I, \ldots, M^{N_g}\right)$, where $N$ is the total number of grains within the polycrystalline model. A separate crystal plasticity finite element simulation needs to be conducted to obtain such an information, which will not be elaborated here. It should be noted that the Coble creep is integrated into the following cavity growth process; hence this mechanism is not needed explicitly.

### 3.2. The smear-out failure model

On accounts of the spherical-caps shape, grain boundary cavities are often depicted by the shape parameters including radius $a$, half-spacing $b$, and cavity tip angle $\psi$ as Fig. 2(a) shows. Onck et al. (Onck and Van der Giessen, 1997) suggest that the cavity tip angle $\psi$ should be about 75° during the growth of cavities. The cavity volume $V$ is described by

$$V = \frac{4}{3}\pi a^3 h(\psi). \tag{17}$$

Here $h(\psi)$ is the spherical-caps shape parameter, which is formulated by

$$h(\psi) = \frac{\left[(1+\cos\psi)^{-1} - 1\Big/2\cos\psi\right]}{\sin\psi}. \tag{18}$$

As shown in Fig. 2(b), Rice introduced a method for grain boundary cavities in a smeared-out sense (Rice, 1981), which enables the model to be substituted by a continuous varying separation $u_n = V/(\pi b^2)$, when reckoning with the complexity of the specific modelling on each individual cavity on grain boundaries. After the simplification, the rate of normal separation can be conveyed by the term of volumetric growth rate $\dot{V}$ of the cavities and the term of the rate of change of the cavity spacing $\dot{b}$,

$$\dot{u}_n = \frac{\dot{V}}{\pi b^2} - \frac{2V\dot{b}}{\pi b^3}. \tag{19}$$

### 3.3. Cavity nucleation and growth

Regarding the cavity nucleation, a physically based understanding for the mechanism is still lacking now. Consequently, a phenomenological model in Tvergaard's work (Tvergaard, 1984) is selected here. When $\sigma_n > 0$, the cavity nucleation rate is

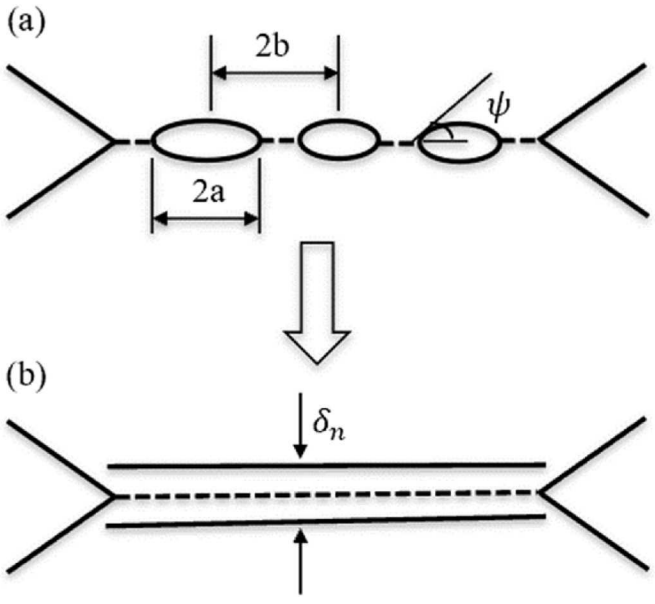


**Fig. 2.** Schematic plots for (a) a number of spherical-cap-shaped cavities located on the grain boundaries and (b) the smeared-out representation of grain boundary cavitation in terms of a continuous varying separation.

$$\dot{N} = F_n \left(\frac{\sigma_n}{\Sigma_0}\right)^2 \dot{\varepsilon}_e^c, \tag{20}$$

here $F_n$ is the material parameter which shows the effect of microstructural features, $\Sigma_0$ is a reference stress, $\sigma_n$ is the normal stress near the grain boundary and $\dot{\varepsilon}_e^c$ is the effective creep rate in the form of $\dot{\varepsilon}_e^c = \dot{\varepsilon}_0(\sigma_e/\sigma_0)^n$, where reference strain rate $\dot{\varepsilon}_0 = A_{dis}\frac{EbD_l}{k_B T}$. Onck et al. (Onck and Van der Giessen, 1998a; Onck and Van der Giessen, 1998b; Onck and Van der Giessen, 1998c) proposed the parameter as the function of stress and strain accumulation,

$$S = \left(\frac{\sigma_n}{\Sigma_0}\right)^2 \varepsilon_e^c \; for \; \sigma_n > 0. \tag{21}$$

It appears to reach a threshold value $S_{thr} = \frac{N_i}{F_n}$, at which cavity nucleation is initiated. Here $N_i$ is the initial cavity density. And the cavity spacing will decrease as stated by

$$\frac{\dot{b}}{b} = \frac{1}{2}(\dot{\varepsilon}_I + \dot{\varepsilon}_{II}) - \frac{1}{2}\frac{\dot{N}}{N}, \tag{22}$$

as cavities keep nucleating on grain boundaries. Here $\dot{\varepsilon}_I$ and $\dot{\varepsilon}_{II}$ are in-plane principle logarithmic strain rate at the grain boundary.

According to the pioneering work of Needleman and Rice (1980), grain boundary diffusion and dislocation creep deformation both contribute to the volumetric cavity growth, which are defined respectively as

$$\dot{V}_1 = 4\pi D \frac{\sigma_n - (1-f)\sigma_s}{\ln(1/f) - \frac{1}{2}(3-f)(1-f)}, \tag{23}$$

$$\dot{V}_2 = \begin{cases} \pm 2\pi\dot{\varepsilon}_e^c a^3 h(\psi)\left[\alpha_n\left|\frac{\sigma_m}{\sigma_e}\right| + \beta_n\right]^n & \text{for } \pm\frac{\sigma_m}{\sigma_e} > 1 \\ 2\pi\dot{\varepsilon}_e^c a^3 h(\psi)(\alpha_n + \beta_n)^n \frac{\sigma_m}{\sigma_e} & \text{for } \left|\frac{\sigma_m}{\sigma_e}\right| < 1 \end{cases}, \tag{24}$$

Here $\sigma_s$ is the sintering stress, $\alpha_n = 3/(2n)$ and $\beta_n = (n-1)(n+0.4319)/n^2$. $f$ is the effective cavity volume fraction is formulated by

$$f = \max\left[\left(\frac{a}{b}\right)^2, \left(\frac{a}{a+1.5L}\right)^2\right], \tag{25}$$

As a stress and temperature dependent material length scale, $L = \left(D\frac{\sigma_e}{\dot{\varepsilon}_e^c}\right)^{1/3}$ shows the contribution to the cavity growth from the coupling of creep deformation and grain boundary diffusion (Rice, 1979).

The effect of dislocation creep is trivial when $L$ is larger than radius a. On the contrary, the cavity growth is gradually dominated by dislocation creep as $L$ becomes smaller. And $D$ is the grain boundary diffusion parameter as follows:

$$D = \frac{D_{b0}\delta_b \Omega}{k_B T}\exp\left(\frac{-Q_b}{RT}\right), \tag{26}$$

where $Q_b$ is the activation energy of grain boundary diffusion, $D_{b0}\delta_b$ is the grain boundary diffusion coefficient and $\Omega$ is the atom volume. Hence the cavity growth rate can be attained by

$$\dot{a} = \dot{V} / \left(4\pi a^2 h(\psi)\right). \tag{27}$$

### 3.4. Grain boundary sliding

Grain boundary sliding (GBS) follows a Newtonian viscous law (Ashby, 1972) and is essentially a thermally activated process, governed by

$$\dot{u}_t = \frac{\Omega\eta_0 \exp(-Q_{gbs}/RT)}{k_B T}\sigma_t. \tag{28}$$

Here $\dot{u}_t$ is the relative sliding velocity of adjoining grains triggered by the shear stress $\sigma_t$ in the grain boundaries, $\eta_0$ is a characteristic sliding velocity and $Q_{gbs}$ is the activation energy for grain boundary sliding. It is also one of the competing mechanisms on creep deformation and damage (Abe et al., 2008; Kimmins and Smith, 1998).

### 3.5. Numerical implementation

By substituting Eqs. (20), (22)–(24) into Eq. (19), the normal separation rate can be derived as function of the normal traction,

$$\dot{u}_n = C_2\sigma_n^2 + C_1\sigma_n + C_0, \tag{29}$$

where

$$C_2 = \frac{V}{\pi b^2}\frac{1}{N}\frac{F_n}{\Sigma_0^2}\dot{\varepsilon}_e^c, \tag{30}$$

$$C_1 = \frac{1}{\pi b^2}\frac{4\pi D}{\ln(1/f) - \frac{1}{2}(3-f)(1-f)}, \tag{31}$$

$$C_0 = \frac{\dot{V}_2}{\pi b^2} - \frac{V}{\pi b^2}(\dot{\varepsilon}_I + \dot{\varepsilon}_{II}) \tag{32}$$

The three terms on the right side of Eq. (29) represent contributions of cavity nucleation, grain boundary diffusion and the creep deformation to the total normal separation of the grain boundary. Combining Eq. (28) with Eq. (29), the material Jacobian matrix is obtained as

$$\begin{Bmatrix} \Delta\sigma_n \\ \Delta\sigma_t \end{Bmatrix} = \begin{bmatrix} \frac{1}{(2C_2\sigma_n + C_1)\Delta t} & 0 \\ 0 & \frac{k_B T}{\Omega\eta_0 \exp(-Q_{gbs}/RT)\Delta t} \end{bmatrix} \begin{Bmatrix} \Delta u_n \\ \Delta u_t \end{Bmatrix} \tag{33}$$

This is what is needed in the finite element implementation as explained in the next section.

## 4. Simulation approach

### 4.1. Finite element method

Based on our previous work (Zhang et al., 2020; Pu et al., 2017), the microstructure-informed and micromechanics-based model is implemented in a commercial finite element software, Abaqus, through user defined subroutines. To simulate the dislocation creep within grain interiors in Eqs. (15) and (16), a user-defined material subroutine (UMAT) is applied in this model. Besides, to study the grain boundary cavitation and growth and GBS under HTHA, a rate-dependent cohesive element is developed by implementing a user-defined element subroutine (UEL). These two subroutines need to be coupled: stress induced diffusion is affected by local stress from both grain boundaries and adjacent grains, and simultaneously, the transporting hydrogen can deteriorate grain boundaries and thus alter stress field of grain interiors. To be more specific, as Fig. 3 shows, the total internal pressure including hydrogen partial pressure and methane partial pressure is regarded as an applied force (i.e., hydrostatic stress $p$) superposed on the applied stress state in cohesive elements and thus integrated into the residual vector in UEL by substituting $\sigma_n$ by $\sigma_n - p$ (Van der Burg and Van der Giessen, 1997; Van der Burg et al., 1998). The adoption of $pa^2/b^2$ is not justified from the linear superposition scheme in Fig. 3.

To illustrate how user-defined cohesive elements are coupled with two neighboring grains, Fig. 4 shows a sketch of the finite element mesh, where three adjacent grains are zoomed in to display the cohesive elements and hydrogen flows along the grain boundaries. The grain interiors are segmented by 4-node hybrid elements with reduced integration under hourglass control (CPE4RH) to simulate the deformation in the grain interiors. The 4-node cohesive elements are added

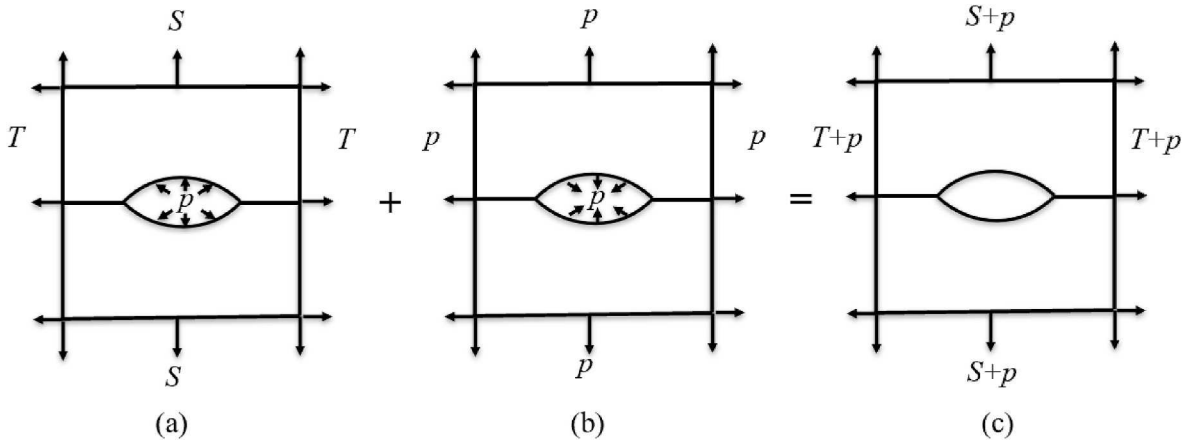


**Fig. 3.** Schematic illustrations of the stress state for a unit cell containing a single cavity under HTHA in (a) and that with an applied hydrostatic tension in (b). Superposing (a) and (b) leads to the stress state in (c) with a stress-free cavity (Van der Burg and Van der Giessen, 1997; Van der Burg et al., 1998).

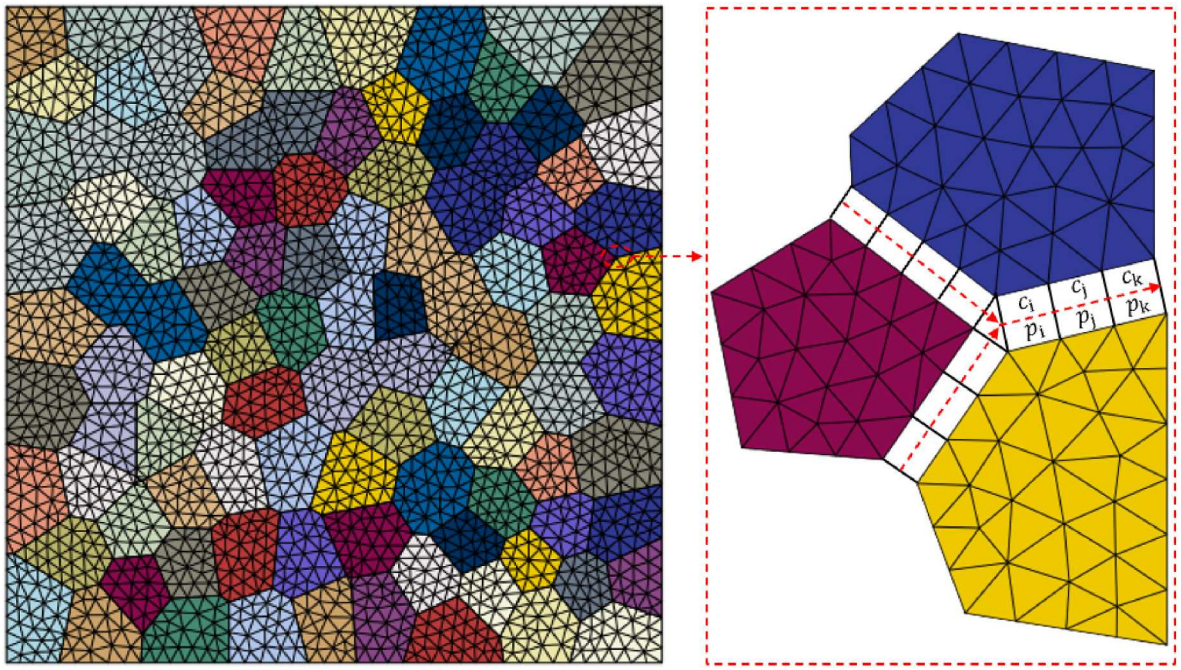


**Fig. 4.** Schematic illustration of the finite element mesh and the concentration-dependent cohesive elements between two neighboring grains. The initial separation in these cohesive elements is zero. Concentration and pressure information are stored in each cohesive element.

on each grain boundary to simulate crack initiation and growth, together with hydrogen diffusion at the meantime. In the unstressed state, the corresponding nodes of the cohesive element are initially aligned together. When an external load is applied, it induces both normal and tangential stresses on the faces of the element. These stresses, in turn, lead to interface separations, governed by the constitutive laws mentioned in Sections 3.2 to 3.5.

In order to gather the essential values for hydrogen diffusion and simulate creep fracture behavior, COMMON BLOCKs are used for data storage and acquisition within the UMAT and UEL subroutines. Specifically, these blocks store details such as pressure and concentration relating to hydrogen diffusion, as well as information concerning state variables in creep fracture. The state variables are retained when the UMAT subroutine is engaged to compute the deformation within the grain interior. Subsequently, these variables are accessed by the UEL subroutine to calculate the development of creep fracture along the grain boundaries.

The stress-coupled diffusion equation Eq.(5) is solved by finite difference (FD) method with a uniform increment,

$$\frac{c_j^{n+1}-c_j^n}{\Delta t}=D\left[\frac{c_{j+1}^n-2c_j^n+c_{j-1}^n}{(\Delta x)^2}+\frac{\overline{V}_H}{RT}\frac{\left(c_{j+1}^n-c_{j-1}^n\right)\left(p_{j+1}^n-p_{j-1}^n\right)}{4(\Delta x)^2}+\frac{\overline{V}_H c_j^n}{RT}\frac{p_{j+1}^n-2p_j^n+p_{j-1}^n}{(\Delta t)^2}\right] \tag{34}$$

where $c_j^n$ and $p_j^n$ denote the concentration and pressure respectively at the $j_{\text{th}}$ element and the $n_{\text{th}}$ time increment. Considering the pressure definition in the 2D cohesive element, $p$ is equal to $-(\sigma_n - P_{total})$, where $P_{total} = P_{H_2} + P_{CH_4}$. Therefore, there are two different time steps from finite difference method and finite difference method (FEM) in this coupled model. The FEM time step as automatically computed and provided to UMAT and UEL is generally much larger than the FD time step, so that this asynchronous step of Eq. (34) needs to be conducted within UEL. These two steps and their communications through the COMMON BLOCKs are illustrated in the appendix (Fig. A).

### 4.2. Material parameters

The material parameters for hydrogen diffusion are listed in Table 1. Diffusion coefficient, activation energy for diffusion, partial molar volume of hydrogen, solubility coefficient, activation energy for solubility are taken from Chavoshi et al.'s work (Chavoshi et al., 2020). For creep fracture, when average grain size is 0.3 mm, the values of materials properties are listed in Table 2. Among these parameters, the reference stress $\Sigma_0$ is taken as that suggested by Onck et al. (Onck and Van der Giessen, 1998a; Onck and Van der Giessen, 1998b; Onck and Van der Giessen, 1998c). Initial cavity radius $a_0 = 6.7 \times 10^{-4}\, R_0$, where $R_0$ is the average grain size. Initial half-spacing $b_0 = 0.16\, R_0$ (Zhang et al., 2020). Young's modulus at different temperatures can be attained by linear interpolation of data from the literature (Chavoshi et al., 2020). The sintering stress $\sigma_s$ is usually relatively small and can be neglected. The stress exponent $n$, reference strain rate $\dot{\varepsilon}_0$, cavity nucleation parameter $F_n$, grain boundary diffusion parameter $D$ are determined via calibration with the experimental creep data for C-0.5Mo steel. These parameters are crucial in governing the relative contribution of characteristic time scales of nucleation, diffusion, and creep deformation.

## 5. Results and discussion

### 5.1. Calibration of creep deformation

To account for the microstructural heterogeneities inherent in C-0.5Mo steel, a two-dimensional digital microstructure is constructed in an open-source software NEPER utilizing the Voronoi tessellation, as illustrated in Fig. 4. The digital microstructure aligns closely with the experimental sample in terms of its topological and structural attributes. The creep strain rate versus stress curve and the creep rupture data from NIMS (National Institute of Materials Research (NIMS) and Japan, 2003) serves as the reference dataset for calibrating the unknown material parameters in the computational model.

As illustrated in Fig. 5(a), we can only perform the calibration of the material parameters for dislocation creep in the high-stress regime by matching the power-law creep rate with experimental data due to lack of Coble creep (diffusional creep) data. The stress exponent for dislocation creep, represented by the slope of the plot, is identified to be approximately 7.79. And the creep rupture data without enough long-term rupture data for C-0.5Mo steel (National Institute of Materials Research (NIMS) and Japan, 2003) is depicted in Fig. 5(b), serving to calibrate the material parameters ($F_n$ and $D$). The numerical outcomes concerning the creep rupture life align quantitatively with the experimental findings. At high temperature and low applied stress, the governing failure mechanism is diffusion-controlled grain boundary cavity growth, so that the stress$\sim 1/T$ plot, converted from Fig. 5(b), should have a slope of $Q_b/R$ with $Q_b$ being the activation energy for grain boundary diffusion and $n = 1$ in this case. At intermediate temperature and high applied stress, failure is controlled by grain-boundary cavity growth driven by dislocation creep deformation of the surrounding grains, so that the slope of the stress$\sim 1/T$ plot should be $Q_l/nR$ with $Q_l$ being the activation energy for lattice diffusion and $n > 1$ in this case. The piecewise nature in Fig. 5(b) support such a transition of failure mechanisms and can be used to derive the activation energies in Table 2. It should be noted that variations in the dataset can be observed, which can be attributed to differences in heat treatment conditions, material compositions, and other factors.

**Table 1**
Representative values for material parameters used for stress-induced hydrogen diffusion model.

| Parameter | Value |
|---|---|
| Diffusion coefficient, $D_0$ | $2.53 \times 10^{-7}\text{m}^2/\text{s}$ |
| Activation energy for diffusion, $\Delta E$ | 13030J/mol |
| Partial molar volume of hydrogen, $\overline{V}_H$ | $2000\text{mm}^3/\text{mol}$ |
| Solubility coefficient, $S_0$ | $0.167\text{mol}/(\text{m}^3\sqrt{\text{Pa}})$ |
| Activation energy for solubility, $\Delta G$ | 21100J/mol |

**Table 2**
Representative values for material parameters used for creep fracture model.

| Parameter | 623 K | 673 K | 723 K | 773 K | 823 K |
|---|---|---|---|---|---|
| Reference stress, $\Sigma_0$ (MPa) | 100 | 100 | 100 | 100 | 100 |
| Average grain size, $R_0$ (mm) | 0.3 | 0.3 | 0.3 | 0.3 | 0.3 |
| Young's modulus, $E$ (GPa) | 179.9 | 169.4 | 158.9 | 148.4 | 137.9 |
| Lattice diffusion, $Q_l$ (kJ/mol) | 450 | 450 | 450 | 450 | 450 |
| GB diffusion, $Q_b$ (kJ/mol) | 174 | 174 | 174 | 174 | 174 |
| Stress exponent, $n$ | 7.79 | 7.79 | 7.79 | 7.79 | 7.79 |
| Reference strain rate $\dot{\varepsilon}_0$ ($\text{s}^{-1}$) | $1.23 \times 10^{-18}$ | $7.85 \times 10^{-16}$ | $2.04 \times 10^{-13}$ | $2.59 \times 10^{-11}$ | $1.82 \times 10^{-9}$ |
| Cavity nucleation parameter, $F_n$ | $4 \times 10^5$ | $4 \times 10^5$ | $4 \times 10^5$ | $4 \times 10^5$ | $4 \times 10^5$ |
| GB diffusion parameter, $D$ ($\text{mm}^5\text{N}^{-1}\text{s}^{-1}$) | $8.64 \times 10^{-20}$ | $1.05 \times 10^{-18}$ | $9.00 \times 10^{-18}$ | $5.85 \times 10^{-17}$ | $3.03 \times 10^{-16}$ |
| Reference stress, $\sigma_0$ (MPa) | 100 | 100 | 100 | 100 | 100 |

### 5.2. Simplifying Nelson curves with Odette-Vagarali model

The Nelson curves provide a comprehensive overview of PVP performance in regards of HTHA, showcasing a series of results across diverse temperatures and hydrogen partial pressures. It distinctly marks the various modes of damage (i.e., surface decarburization, fissuring, and material decarburization) on the depicted equipment data points. Nelson curves play an integral role in the design and fabrication of pressure vessels and pumps operating at temperatures above 205 °C and hydrogen pressures exceeding 690 KPa. They delineate the operational boundaries for specific steels when used in high-temperature hydrogen environments.

As previously explained in Fig. 1(b), there is a lack of piece-wise characteristics in the hydrogen partial pressure versus the reciprocal of temperature plot, with some particular obscure features along the tails of these curves at low pressure and high temperature. Considering the Odette-Vagarali model and the total pressure (summing hydrogen and methane partial pressures) being the applied load as shown in Fig. 3, we now convert Nelson curves further to the plot in Fig. 6. Within a wide range of temperatures (from 773 K to 1173 K), the methane partial pressure varies rapidly with respect the initial increase of the hydrogen partial pressure, but slows down at the later stage, as shown in Fig. 6(a). It is evident that the fitted expressions in Eqs. (6) and (13) of the temperature dependent coefficient $C(T)$ results in sudden sharp discontinuities at the transitions, but these jumps are small and will not affect our results. Eventually, by combining Figs. 1(b) and Fig. 6(a), we can obtain a final converted Nelson curves in Fig. 6(b), which could be delineated into two distinct regimes, i.e., dislocation-creep-controlled or grain boundary diffusion-assisted cavity growth. And there is a clear

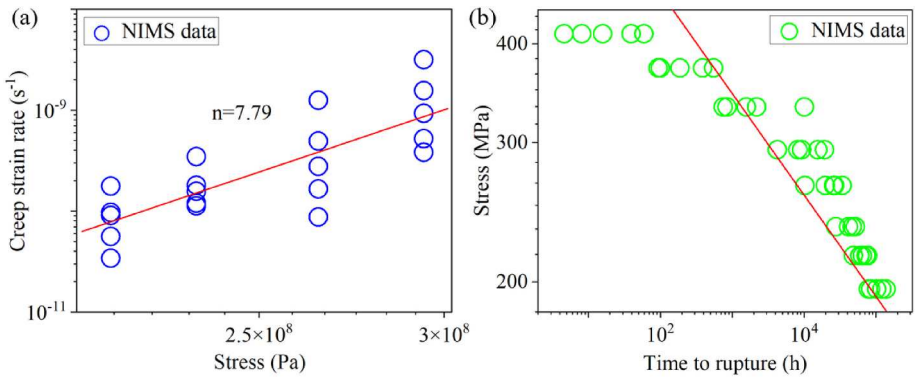


**Fig. 5.** (a) Stress dependence of steady state creep rate for C-0.5Mo steel at 723 K. (b) Stress vs. creep life behavior predicted using the micromechanical model for PVP of C-0.5Mo steel in comparison with the literature experimental data at 723 K. NIMS data are obtained from (National Institute of Materials Research (NIMS) and Japan, 2003).

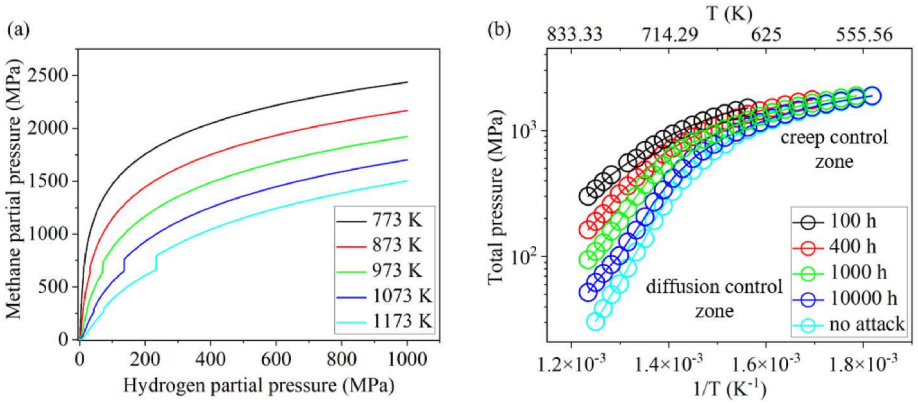


**Fig. 6.** (a) Predicted equilibrium methane partial pressure from 773 K to 1173 K according to Odette-Vagarali model (Odette and Vagarali, 1982). (b) Final converted Nelson curves by combining (a) and Fig. 1(b).

transition from creep control region to diffusion control region at about 700 K.

### 5.3. HTHA with uniform hydrogen distribution (equivalent to ultrathin wall)

To further investigate the Nelson curves, here we study a special case in which the pipeline steel is thin enough so that the hydrogen distribution is uniform across the thickness and takes the value of Eq. (4). Using the Odette-Vagarali model gives the methane pressure, which thus provides inputs to the creep fracture model (e.g., Eqs. (23) and (24)). Assuming an initial ratio of $a/b$ and integrating these ODEs, we can calculate the separation vs time curve of only one grain boundary lying normal to the loading direction. The lifetime is determined from the catastrophic growth of the separation, corresponding to the cavity coalescence stage. An interpolation is needed to find out the critical stress (or hydrogen partial pressure) to reach a given lifetime (e.g., 100 h in Fig. 7). From this method, a series of simulations are performed under

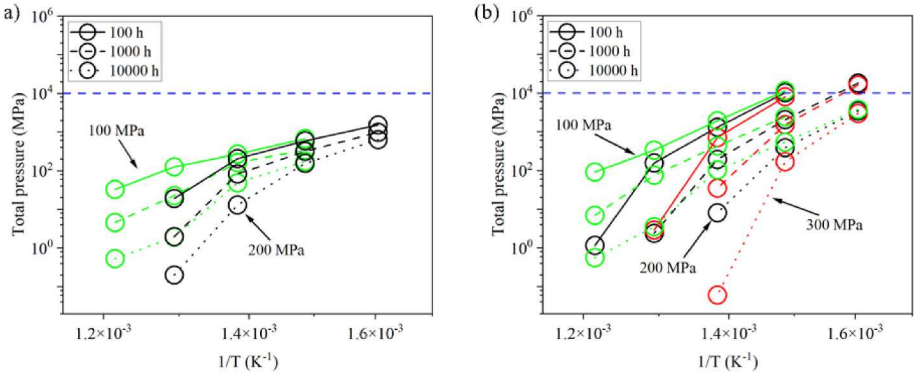


**Fig. 7.** Predicted Nelson curves with total pressure and the reciprocal of temperature under HTHA with uniform hydrogen distribution, obtained from solving a set of ordinary differential equations (ODE model) under external loading of 100 MPa and 200 MPa in (a), and from finite element method (FEM) under external loading of 100 MPa, 200 MPa and 300 MPa in (b). The differences lie on the nature of statistical averages in FEM. The grain size (i.e., ledge size of the hexagonal grain) is 300 $\mu m$.

external loading of 100 MPa and 200 MPa within a temperature range from 623 K to 823 K. Alternatively, we can employ the FEM in Section 4 with a constant total pressure calculated from the Odette-Vagarali model. Results from both methods are given in Fig. 7(a) and (b), respectively, in the plots of total pressure versus temperature with contour lines denoting a certain lifetime. The contrast of these two subfigures clearly results from the statistical average of grain boundaries oriented in all possible directions in Fig. 4. It should be noted that the transition temperature at which the slope changes rapidly is similar in both results, because this transition results from the competition between diffusive vs creep-constrained cavity growth processes.

Comparing to the converted Nelson curves in Fig. 6(b) (compiled from experimental observations), our FEM results in Fig. 7(b) underpredicts at high temperature but overpredicts at low temperature, both by about one order of magnitude. The transition temperature is again well predicted. Again, in addition to a wide range of unknown applied stress, experimental data in Fig. 1(a) also have many unknown factors, such as wall thickness, microstructural information (that might considerably change parameters in Tables 1 and 2), failure locations (some literature indicating failure occurring at weldments), or others. Since hydrogen concentration is assumed to be constant through the thickness, our results exaggerate its contribution to the final failure. The role of thickness will be studied in the next subsection.

### 5.4. HTHA with nonuniform hydrogen distribution (i.e., thick walls)

Our microstructure-informed and micromechanics-based model solves the transient and coupled behavior of both hydrogen diffusion and intergranular cavity growth, so that the roles of microstructural heterogeneities, distribution of the applied load, gradient of the hydrogen field, and others can be easily investigated. In this work, the hydrogen concentration at the inner diameter surface is determined from the Sieverts law in Section 2.1, and that at the outer surface is taken as zero. As mentioned before, grain boundary diffusivity is usually $10^5 \sim 10^8$ times higher than that inside grain (National Institute of Materials Research (NIMS) and Japan, 2003; Nieh et al., 1997). Thus, only diffusion coefficient $D_0 = 2.53 \times 10^{-7} m^2/s$ with the activation energy for diffusion $\Delta E = 13030 \mathrm{J/mol}$ is adopted in our work.

For a representative thick-wall example, Fig. 8 presents the contour plot of the von Mises stress distribution for the whole sample of C-0.5Mo steel with hydrogen concentration of $10^8$ $atom/\mu m^3$ under 773 K and without any applied stress. HTHA is successfully simulated by using the micromechanics model. Note that the deformation is enlarged for better visualization. Hydrogen diffusion clearly takes time, but as hydrogen penetrates further, localized damage occurs simultaneously which in turns facilitates the hydrogen diffusion into the bulk. In this case, even without applied stress, the resulting stress concentration can be as high as tens of MPas. The crack opening displacement also shows an evident gradient. Simulations were performed with rather uniform properties on the grain boundaries. Should there be any microstructural heterogeneities, "hot spots" of microcrack initiation might be found away from the inner diameter. The penetration depth of hydrogen field can be estimated from the characteristic diffusion length,

$$L_d = \sqrt{Dt}, \tag{35}$$

which is about 1 mm in this simulation example. Compared to a grain size of 0.3 mm in this case, it is therefore natural to see the damage layer as deep as a few grains.

The synergistic effects of applied load and PVP wall thickness can be illustrated in Fig. 9. Further parametric studies beyond the representative example in Fig. 8 need to be performed with varying temperature and applied stress, giving rise to the total pressure versus lifetime curves in Fig. 9(a). Again, an interpolation step is needed to find the critical

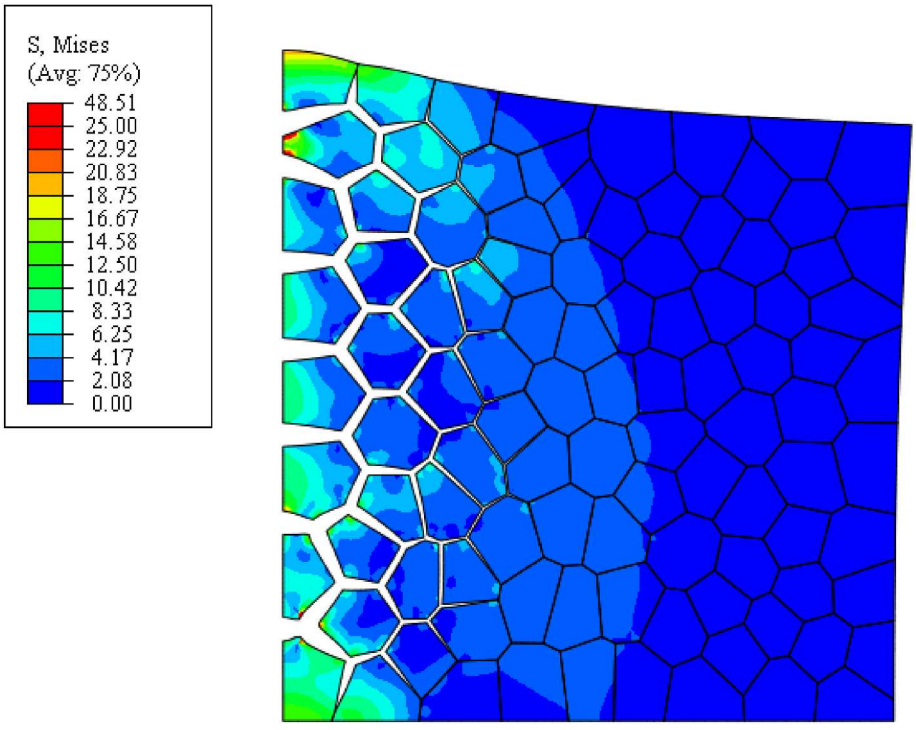


**Fig. 8.** Contour plot of the von Mises stress distribution in the PVP of C-0.5Mo steel by 100-grain structure. Typical failure occurs under HTHA with a very thick wall, so that hydrogen does not penetrate to the outer diameter. Here, the left side is the inner diameter (exposed to hydrogen) and the right side is the outer diameter. The left surface is fixed with horizontal displacement, while the bottom surface is fixed with vertical displacement. A magnification ratio of 2000 is used here for the displacement field to illustrate the microcracks clearly. Simulation parameters include those listed in Tables 1 and 2, together with T = 773 K, no applied stress, grain size of 300 $\mu m$, and hydrogen concentration at inner diameter of $10^8$ $atom/\mu m^3$. The snapshot was taken near the final failure when the vertical elongation increases catastrophically.

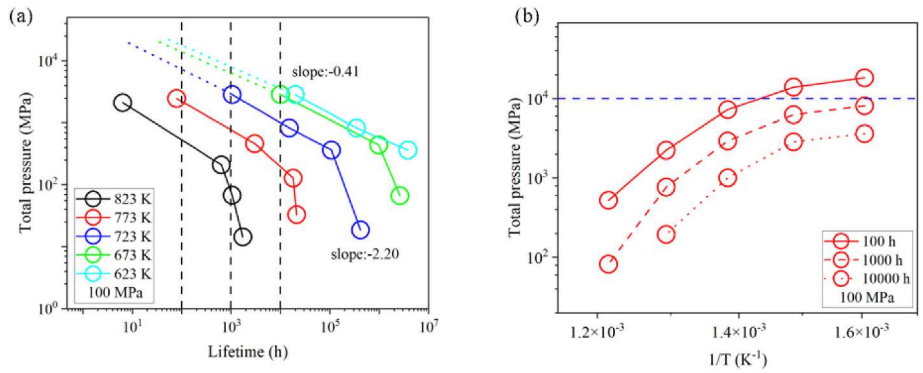


**Fig. 9.** (a) Total pressure vs. creep rupture time under HTHA with nonuniform hydrogen distribution by our coupled model for 100 MPa. (b) Predicted Nelson curves with total pressure and the reciprocal of temperature under HTHA with a thick wall for 100 MPa. The grain size is 300 $\mu m$.

total pressure for a given lifetime such as 100 h, as shown by the vertical dashed lines there. The resulting Nelson curves in Fig. 9(b) show a clear contrast to uniform-hydrogen-field results in Fig. 7(b) as described below. First, the transition from diffusive to creep-controlled cavity growth can still be seen from the slope change, but these slope values are heavily affected by external loading (not being equal to stress exponent in creep control region or to unity 1 in diffusion control region). Second, the range of the calculated total pressure for a lifetime change from 100 h to 10,000 h is much more reduced here when compared to Fig. 7(b). This agrees favorably with the experimental Nelson curves in Fig. 6(b). Third, combining the calculation results in Fig. 7(b) and 9(b), it is therefore derived that a favorable agreement with the experimental Nelson curves in Fig. 6(b) can only be made for a thick wall with some moderate applied stress, provided with a carefully calibrated set of material parameters.

For brevity, this work does not include additional simulations on the role of grain size and microstructural heterogeneities. While these lines of information are not known in the API Nelson curves, we have conducted a number of HTHA experiments under bending tests, which illustrate various fracture morphologies with respect to microstructural heterogeneities. The grain size changes the NIMS data (e.g., Fig. 5) dramatically, so that it is anticipated that the corresponding Nelson curves (e.g., Figs. 7 and 9) will change accordingly. Any experimental validation will therefore require a fine knowledge of material microstructure and grain size, which are not known in the present Nelson curves.

## 6. Summary

A fully coupled micromechanical model has been developed to investigate both the thermodynamic/kinetic processes of hydrogen and the simultaneous cavity growth, from which the failure lifetime can be obtained with respect to variables such as microstructural heterogeneities, load distributions, geometrical feature sizes, and prior residual stress fields. These predictions can be used to construct the Nelson curves, which delineates the safety design regimes in the plot of the hydrogen partial pressure with respect to the temperature. While the converted Nelson curves can clearly exhibit two stages, as governed by diffusive cavity growth or by creep-constrained cavity growth, the computed Nelson curves underpredict at high temperature and low stress but overpredict at intermediate temperature and high stress. These numerical predictions are found to be sensitive to applied stress and PVP wall thickness, and potentially to variations of constitutive parameters that are sensitive to microstructural heterogeneities. A comprehensive parametric study and a complete knowledge of boundary/initial conditions and material properties are certainly the prerequisite for a quantitative assessment of Nelson curves, despite our ability to delineate the governing creep failure mechanisms.

## CRediT authorship contribution statement

**Dong Han:** Conceptualization, Data curation, Formal analysis, Investigation, Methodology, Project administration, Resources, Software, Validation, Visualization, Writing – original draft, Writing – review & editing. **Yanfei Gao:** Conceptualization, Data curation, Formal analysis, Funding acquisition, Investigation, Methodology, Project administration, Resources, Software, Supervision, Validation, Visualization, Writing – original draft, Writing – review & editing. **Phillip E. Loya:** Conceptualization, Data curation, Formal analysis, Investigation, Methodology, Project administration, Resources, Software, Validation, Visualization, Writing – original draft, Writing – review & editing. **Michael Swindeman:** Conceptualization, Data curation, Formal analysis, Investigation, Methodology, Project administration, Resources, Software, Validation, Visualization, Writing – original draft, Writing – review & editing. **Jorge Penso:** Conceptualization, Data curation, Formal analysis, Investigation, Methodology, Project administration, Resources, Software, Validation, Visualization, Writing – original draft, Writing – review & editing. **Zhili Feng:** Conceptualization, Data curation, Formal analysis, Funding acquisition, Investigation, Methodology, Project administration, Resources, Software, Supervision, Validation, Visualization, Writing – original draft, Writing – review & editing.

## Declaration of competing interest

The authors declare no conflict of interest in this manuscript.

## Data availability

Data will be made available on request.

## Acknowledgments

This work was financially supported by the NSF Industry University Cooperative Research Center (I/UCRC) program, to the University of Tennessee under the Manufacturing and Materials Joining Innovation Center (Ma2JIC) with IIP 1540000 and IIP 1822186. DH also acknowledges the support from Center for Materials Processing at the University of Tennessee.

## Appendix A

A schematic illustration of the coupled model (Fig. A) is introduced in Section 4.1 to clarify the specific implementation of the hydrogen diffusion and cavity growth model within the finite element framework. This sets the algorithm used in the UEL subroutine.

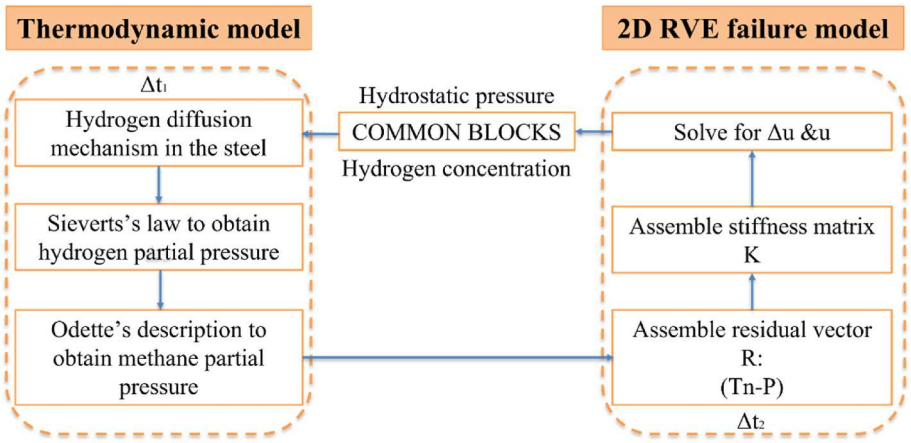


**Fig. A.** A schematic illustration of the coupled model: left being the thermodynamic calculation of hydrogen transport, and right showing the steps for cavity-induced failure. These two modules have different time steps, but communicate through a number of COMMON BLOCKs.

## References


Abe, F., Kern, T.U., Viswanathan, R. (Eds.), 2008. Creep-Resistant Steels. Elsevier.

American Petroleum Institute, 2016. Steels for Hydrogen Service at Elevated Temperatures and Pressures in Petroleum Refineries and Petrochemical Plants.

Argon, A.S., 1983. Mechanisms and mechanics of fracture in creeping alloys. Pineridge Press, Recent Advances in Creep and Fatigue of Engineering Materials and Structures 1–52.

Ashby, M.F., 1972. Boundary defects, and atomistic aspects of boundary sliding and diffusional creep. Surf. Sci. 31, 498–542.

Bharadwaj, M., 2015. Studies of High Temperature Hydrogen Related Damage in Welded Carbon Steel Components Used in Refineries. PhD Thesis. University of Tennessee.

Chavoshi, S.Z., Hill, L.T., Bagnoli, K.E., Holloman, R.L., Nikbin, K.M., 2020. A combined fugacity and multi-axial ductility damage approach in predicting high temperature hydrogen attack in a reactor inlet nozzle. Eng. Fail. Anal. 117, 104948.

Cocks, A.C.F., Ashby, M.F., 1982. On creep fracture by void growth. Prog. Mater. Sci. 27, 189–244.

D Van der Burg, M.W., Van der Giessen, E., Brouwer, R.C., 1996. Investigation of hydrogen attack in 2.25 Cr-1Mo steels with a high-triaxiality void growth model. Acta Mater. 44, 505–518.

Dadfarnia, M., Martin, M.L., Moore, D.E., Orwig, S.E., Sofronis, P., 2019. Model for high temperature hydrogen attack in carbon steels under constrained void growth. Int. J. Fract. 219, 1–17.

Fisher, J.C., 1951. Calculation of diffusion penetration curves for surface and grain boundary diffusion. J. Appl. Phys. 22, 74–77.

Gandhi, C., Ashby, M.F., 1979. Fracture-mechanism maps for materials which cleave: FCC, BCC and HCP Metals and ceramics. Acta Metall. 27, 1565–1602.

Kimmins, S., Smith, D., 1998. On the relaxation of interface stresses during creep of ferritic steel weldments. J. Strain Anal. Eng. Des. 33, 195–206.

National Institute of Materials Research (NIMS), Japan, 2003. In: Proceedings of the NIMS Creep Data Sheet.

Needleman, A., Rice, J.R., 1980. Plastic creep flow effects in the diffusive cavitation of grain boundaries. Acta Metall. 28, 1315–1332.

Nelson, G.A., 1977. Hydrogenation plant steels. In: Beachem, C.D. (Ed.), Hydrogen Damage. American Society for Metals, pp. 377–394.

Nieh, T.G., Wadsworth, J., Sherby, O.D., 1997. Superplasticity in Metals and Ceramics. Cambridge University Press.

Odette, G.R., Vagarali, S.S., 1982. An equation-of-state for methane for modeling hydrogen attack in ferritic steels. Metall. Trans. A 13, 299–303.

Onck, P., Van der Giessen, E., 1997. Microstructurally-based modelling of intergranular creep fracture using grain elements. Mech. Mater. 26, 109–126.

Onck, P., Van der Giessen, E., 1998a. Growth of an initially sharp crack by grain boundary cavitation. J. Mech. Phys. Solid. 47, 99–139.

Onck, P., Van der Giessen, E., 1998b. Micromechanics of creep fracture: simulation of intergranular crack growth. Comput. Mater. Sci. 13, 90–102.

Onck, P., Van der Giessen, E., 1998c. Microstructural modelling of creep crack growth from a blunted crack. Int. J. Fract. 92, 373–399.

Parthasarathy, T.A., 1985. Mechanisms of hydrogen attack of carbon and 214Cr-1Mo steels. Acta Metall. 33, 1673–1681.

Pu, C., Gao, Y.F., Wang, Y., Sham, T.L., 2017. Diffusion-coupled cohesive interface simulations of stress corrosion intergranular cracking in polycrystalline materials. Acta Mater. 136, 21–31.

Rice, J.R., 1979. Time dependent fracture of materials at elevated temperature. US Department of Energy Report 130.

Rice, J.R., 1981. Constraints on the diffusive cavitation of isolated grain boundary facets in creeping polycrystals. Acta Metall. 29, 675–681.

Riedel, H., 2014. Fracture at High Temperatures. Springer.

Schlögl, S.M., Van der Giessen, E., 2002. Computational model for carbon diffusion and methane formation in a ferritic steel during hydrogen attack. Scripta Mater. 46, 431–436.

Shewmon, P., 1987a. Synergism between creep ductility and grain boundary bubbles. Acta Metall. 35, 1317–1324.

Shewmon, P., 1987b. Synergism between creep ductility and grain boundary bubbles. Acta Metall. 35, 1317–1324.

Shih, H., Johnson, H.H., 1982. A model calculation of the Nelson curves for hydrogen attack. Acta Metall. 30, 537–545.

Sieverts, A., 1935. The solubility of deuterium and hydrogen in solid palladium. Z. Phys. Chem. 174, 359–364.

Sundararajan, G., Shewmon, P.G., 1981. The kinetics of hydrogen attack of steels. Metall. Trans. A 12, 1761–1775.

Tvergaard, V., 1984. On the creep constrained diffusive cavitation of grain boundary facets. J. Mech. Phys. Solid. 32, 373–393.

Van der Burg, M.W.D., Van der Giessen, E., 1996. Non-uniform hydrogen attack cavitation and the role of interaction with creep. Mater. Sci. Eng., A 220, 200–214.

Van der Burg, M.W.D., Van der Giessen, E., 1997. A continuum damage relation for hydrogen attack cavitation. Acta Mater. 45, 3047–3057.

Van der Burg, M.W.D., Van der Giessen, E., Viggo, T., 1998. A continuum damage analysis of hydrogen attack in a 2.25 Cr–1Mo pressure vessel. Mater. Sci. Eng., A 241, 1–13.

Vitovec, F.H., 1984. Investigation of models for hydrogen attack of steel. J. Mater. Sci. 19, 2771–2774.

Whipple, R.T.P., 1954. Concentration contours in grain boundary diffusion, London, Edinburgh, Dublin Philos. Mag. J. Sci. 45, 1225–1236.

Zhang, W., Wang, X., Wang, Y., Yu, X., Gao, Y.F., Feng, Z., 2020. Type IV failure in weldment of creep resistant ferritic alloys: II. Creep fracture and lifetime prediction. J. Mech. Phys. Solid. 134, 103775.